



Metallurgical and mechanical attributes of gas metal arc welded high-strength low-alloy steel

Dawei Zhao¹ · Yuriy Bezgans¹ · Nikita Vdonin¹ · Lyudmila Radionova² · Lev Glebov³ · Vitaly Bykov³

Received: 13 October 2022 / Accepted: 1 January 2023 / Published online: 6 January 2023
© The Author(s), under exclusive licence to Springer-Verlag London Ltd., part of Springer Nature 2023

Abstract

The intention of this study is to explore the influences of welding settings upon the geometry, microstructure transformation, and tensile properties of the gas metal arc welded joints of weathering steel ASTM A606 type IV. The individual effect of the welding variables (welding speed, welding current, and wire feed speed) on the geometries of the weld bead and its tensile properties was explored. The characteristics of the microstructure and macrostructure with various technological parameters were also investigated. It is indicated that all the selected welding process parameters significantly affect the welding microstructural and macrostructural features of the welded joints as well as their tensile properties. The results imply that no major defects were observed based on the macrostructure examination. The fusion zone (FZ) changes ferrite and pearlite morphology, relying upon the cooling speed and duration time. The FZ exhibits acicular ferrite, Widmanstatten ferrite, and grain boundary ferrite, resulting in its inferior hardness to that of the coarse grain heat-affected zone (CGHAZ) and weld interface (WI). The adjustment of the welding process parameters bringing about the reduction of the welding heat input contributes to the production of acicular ferrite. The hardness of the weld metal steadily decreases from the heat-affected zone (HAZ) to the base metal (BM). The average tensile strength of the weld metal is 596 MPa, which is comparable to that of the BM. The fracture location is in BM, and the fracture behavior retains ductility. After that, models computing the correlations between welding parameters and welding quality indexes (failure energy of the welded joints, depth of the penetration and bottom reinforcement, and standard derivation of the failure energy) were established and analyzed. The optimal welding parameters were figured out using the desirability approach.

Keywords Operating parameters · Tensile properties · Weld bead profile · Microstructure · Gas metal arc welding

1 Introduction

Weathering steel belongs to the class of high-strength low-alloy (HLSA) steel with low content of carbon and some small amounts of other alloy elements (aluminum, titanium, copper, and so on). This kind of steel has a fantastic combination of favorable merits such as strength, formability, weldability, and ductility. Its yield strength is approximately

three times superior to that of ordinary carbon steel. In addition, this kind of material is able to afford improved atmospheric corrosion resistance. Thanks to its outstanding advantages, weathering steels are largely used in numerous applications such as petrol transportation pipelines, bridge beams, ships, towers, and vessels. Among these various sections, welding is the elementary joining method.

One of the most frequently used welding methods in several industries is gas metal arc welding (GMAW). The GMAW is preferable since it outperforms other welding techniques in many aspects. Its advantages include high efficiency, ease of operation and automation, and low requirements for the operator's skills. During the GMAW process, the welding variables and welding procedures influence and determine the welding quality which in turn plays a major role in the strength of the mechanical parts and components. Understanding and exposing the effects of the welding process variables upon the welding quality are the basic

✉ Dawei Zhao
zhaodawei0322@xy.hfut.edu.cn

¹ Department of Welding Engineering, Institution of Engineering and Technology, South Ural State University, Chelyabinsk 454080, Russia

² Moscow Polytechnic University, Moscow 107023, Russia

³ Department of Metal Forming, Institution of Engineering and Technology, South Ural State University, Chelyabinsk 454080, Russia

knowledge to recommend the suitable welding procedures and settings to obtain the welded joints with decent quality as well as high productivity without sacrificing the reliability of the welding assembly. Some researchers all over the world have done some research regarding this issue. Turner et al. [1] investigated the effects of several welding parameters on the bead geometry of low-carbon steel in the GMAW process. The welding parameters included welding speed, voltage, welding current, and shielding gas, while the geometric features of the weld bead were composed of penetration depth, height, width, the contact angle, hardness, and dilution. With the aim of modeling the relationship between the welding parameters and weld bead profile, the response surface methodology was utilized to establish the models. The effects and interaction effects of the selected welding parameters upon the weld bead geometry were revealed based on these developed models. The optimal combination of the welding parameters was finally decided. Ibrahim et al. [2] chose three different levels of welding current, voltage, and welding speed to investigate their effects on welding penetration, microstructure, and hardness in the weld bead of mild steel with a thickness of 6 mm. The results indicated that the penetration depth increased with the welding current, while the voltage and welding speed were the other factors that significantly influenced the penetration depth. The welding parameters also altered the grain sizes of the welds regarding the microstructure. Rizvi and Tewari [3] performed welding experiments on the stainless steel 304H with various shielding gas flow volume levels, welding current, voltage, and wire feed speed. The tensile tests and V-notch Charpy tests were made use of to express the mechanical attributes of the welds, and the microstructures of different zones were observed via a microscope. The researchers found that the microstructural characteristics and mechanical attributes of the weld bead were adjusted by the shielding gas flow and wire feed speed, while the welding current strongly affected the toughness and strength of the welded samples. Moslemi et al. [4] divided the welding current into four levels to study its influence on the weld bead profile, microstructure, hardness, and tensile shear strength of the welds of 316 stainless steel. All the experimental results specified that the increase of welding current enlarged the welding heat input applied to the weld pool, which in turn brought about larger weld bead width and deeper penetration. In addition, the sigma phase in the matrix accumulated and the chromium carbide percentage declined with the rise of the welding current. According to the experimental work, the optimal level of the welding current figured out could yield the welds with the highest strength and fewest welding defects. Bodude and Momohjimoh [5] carried out the welding experiments with different levels of the welding parameters which were a voltage of 100 V and 220 V and welding current of 100 A, 120 A, and 150 A. The mechanical

attributes of the welded joints were expressed via tensile strength, hardness, and impact strength. The tensile strength and hardness reduced as the welding heat input increased, while the impact strength increased with the same factor. The proportion of ferrite to pearlite varied with different welding parameters. Wang et al. [6] altered the compositions of the welding shielding gas into several levels, namely, pure argon, pure carbon dioxide, and different mixtures of carbon dioxide and argon. The measurement of the weld bead profile indicated that the gas composition strongly influenced the arc temperature profile and heat transfer to the work-piece; all these factors resulted in different weld geometries. Higher carbon dioxide gave rise to a more constricted arc plasma together with higher energy density, which in turn produced a wider and deeper weld pool and reduced reinforcement height. Widianto et al. [7] investigated the influence of welding sequence and welding current on distortion, mechanical properties, and metallurgical observations of the butt joints of SS 316L steel. Three levels of welding current and four levels of welding sequences were chosen. The results hinted that the deformation and distortion of the welded pipe, namely, axial distortion, transverse distortion, ovality, and taper, increased with the welding current, while it first decreased with the welding sequence until getting to its lowest point, and then, it increased with the welding sequences. Only one welding sequence resulted in lower mechanical properties; the value of hardness also decreased when more welding sequence was employed even if the levels of welding current and pipe position were the same. The increase of welding current deepened the penetration, while the penetration depth decreased when adding the welding sequence. Chaudhary and Khanna [8] attempted to develop a mathematical relationship between weld bead parameters and welding parameters for the submerged arc welding technique. The welding speed, voltage, and wire feed rate with different levels were chosen as the welding parameters, while the penetration depth, reinforcement height, and bead width were selected as the weld bead geometry features. The penetration depth highly increased with the wire feed rate and voltage. Varbai et al. [9] investigated the effects of active fluxes on the welding quality of GMAW for carbon steel. In their experimental work, eight different types of active fluxes were employed while the welding quality was expressed by the weld bead profile, hardness distribution, and microstructure. The results implied that the weld bead width was proportionate to the oxygen content in the active flux, while the bead height was oppositely proportional to the same factor. The changes in the bead geometry hardly altered the microstructure and hardness profile of the welded joints. Ley et al. [10] inspected the effect of welding shielding gas upon the post-weld thermal characteristics of the weld in the GMAW process. The factors of the shielding gas included supply method, composition, and flow volume.

The results highlighted that the shielding gas weightily affected the main thermal factors that solidified the weld metal via computational modeling. A lower shielding gas flow rate was beneficial to the welding quality in the terms of a smaller thermal expansion, greater specific heat capacity, and higher thermal conductivity. Wang et al. [11] compared the effects of the commonly used thermal frequencies on the welding process suitability, bead profile, macrostructure, and hardness distribution of the double-pulsed GMAW of AA6061 aluminum alloy. Three levels of thermal frequencies were selected. It was determined that thermal frequency did not alter the welding suitability as the welding parameters were self-matching; the weld ripple, maximum penetration depth, and grain size of the fusion zone (FZ) reduced with the increase in thermal frequency, while the hardness at the FZ increased by the same factor.

Since HSLA steel has many advantages mentioned above, some other researchers have also done some work on the welding of newly developed HSLA steels. Hariprasath et al. [12] investigated the effect of welding process parameters on the mechanical and metallurgical properties of fusion welded DMR249A grade steel. They correlated tensile, impact, and microhardness properties to the microstructure of welded joints. It was found that the failure occurred in the subcritical heat-affected zone (HAZ) due to grain deformation and subsequent softening of the weldment. Ribeiro et al. [13] evaluated the hardness, fracture toughness, and fatigue crack growth of weld beads obtained by two laser welding processes with different heat inputs. The former produced weld beads with different ferrite morphologies, while the latter yielded welded joints with martensite and bainite. They found that fracture toughness was more sensitive to microstructural changes induced by heat input than hardness and fatigue cracks. Vaikar et al. [14] studied the performance of welded joints made of marine-grade HSLA steel with a thickness of 12 mm. The pulsed direct current (PDC) gas tungsten arc welding (GTAW) was employed while the filler metal was ER80S-Ni3. The impact toughness of HSLA joints was greater than that of the base alloy. When the temperature was lowered, the welded joint underwent higher ductility and a transition from a ductile to a brittle fracture mode. Kornokar et al. [15] investigated the effect of heat input during automated GTAW on the microstructure and mechanical properties of HSLA steel S500MC. It was found that the size of martensite increased due to the dissolution of carbides, and the amount of retained austenite also increased with increasing welding heat input. Nouredine and Allaoui [16] studied the effect of tempering on the corrosion behavior of HSLA steel X70 weldment in 1-M sulfuric acid solution. They chose two different temperatures, 450 °C and 650 °C, to study the effect of tempering on the welded samples. It was detected that the mechanical properties were best after tempering and that the polarization resistance enhanced

after tempering via reducing corrosion-inducing factors such as residual stresses. According to previous research work, welding heat input has a profound impact on welding quality, and welding heat input is determined by welding operation parameters. In this case, the influence of welding process parameters on welding quality indicators should be revealed in advance. Only then will the properties of the welded joint be linked to the welding parameters. Then, suitable welding parameters can be found to obtain the welded joints with good quality.

The welding quality of the weathering steel A606 is rather essential in the manufacturing of key mechanical components such as boilers, collecting tanks, and oil pipes. Different welding parameters, for instance, voltage, welding speed, welding current, shielding gas, wire feed speed, and type and size of filling material, affect the physical and mechanical performance of the welded joints. Improper welding parameters may bring about inevitable welding discontinuities that are harmful to the welding quality. Engineers and researchers in the manufacturing industries regularly encounter the problem of choosing the appropriate combinations of welding variables to attain the desired welding quality. To realize this goal, the effects and mechanisms of the welding procedures and parameters on the welding quality (macrostructure, microstructure, weld bead profile, mechanical properties in the mechanical tests, and so on) should be clear in advance. After that, the best welding performance will be attained by establishing the models for welding parameters and welding quality indexes.

2 Experimental detail

Weathering steel (grade A606 type IV) was selected to be butt-joined. The thickness of this material was 3 mm. The size of the steel sheet was 60×50 mm without edge chamfering, as revealed in Fig. 1. During the GMAW process, the gap between the steel sheets was 1.0 mm. Low-alloy structural steel wire (09G2S) whose diameter was 1.2 mm was utilized as the consumable electrode. Table 1 summarizes the chemical compositions of the welded steel and consumable filler wire respectively. Before welding, the welding steel sheets were cleaned with acetone to reduce the detrimental effects of the dirt upon the upper and lower surfaces of the steel sheets upon the welding quality.

As for the welding experiments, a Kemppi KempArc Pulse 450 GMAW machine automated with a Fanuc Robot Arc Mate 120iC was used. The angle of the welding torch was vertical to the welding sheets, and the distance from the electrode tip to the metal sheets was 15 mm. The shielding gas composed of 82% Ar and 18% CO₂ was employed in the weld pool to prevent the weld bead from producing environmental contaminants and oxidation, and its flow rate was 20

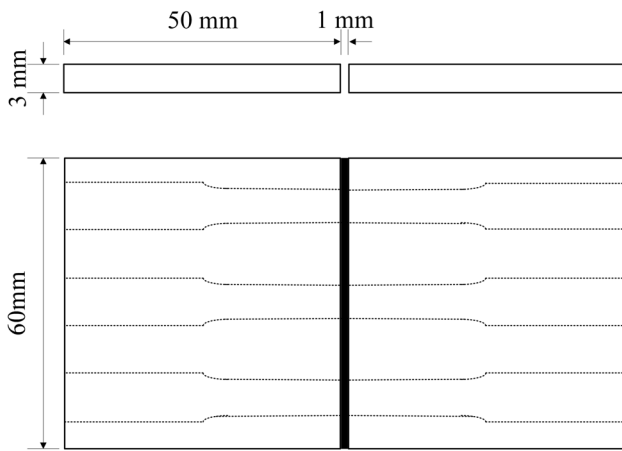


Fig. 1 The dimensions and sizes of the welded samples

L/min. Before welding, the welding plates were clamped and fixed. The selected variable parameters consisted of welding speed, wire feed speed, and voltage.

The macroscopic appearances of the produced welded samples were assessed via visual and microscopic checks. The optical microscope as well as scanning electron

microscope (SEM) was employed to observe the microstructure of the welds produced by different welding process parameters. The samples were first arranged and cut by the wire discharge machine to prepare for the examination of the microstructure and geometrical characteristics of the weld bead. After that, they were mounted in gum resin and then ground with several sheets of diamond sandpaper from 800 to 4000 grits. The samples were then polished with 0.5- μm alumina suspension and etched with 4% nitric acid for a few seconds to display the microstructure of the welds.

The microhardness distributions throughout the weld zone were estimated on the metallographic specimens via the micro-Vickers hardness tests. The hardness tests were performed along a line perpendicular to the welding line and across the FZ, weld interface (WI), HAZ, and BM. The intervals of the spots for the hardness tests are 0.3 mm, while the load is 100 g.

The welded specimens for the tensile shear tests were cut along the longitudinal line, which is vertical to the welding line. The size of the tensile samples with a notch and without a notch is exhibited in Fig. 2. The tests were executed under the quasi-static circumstance with a constant loading speed of 5 mm/min.

Table 1 Chemical compositions (wt. %) and mechanical properties of base metal (BM) and 09G2S steel

	Chemical compositions											Mechanical properties		
	C	Mn	Cr	Al	Si	Cu	Ni	P	Mo	V	S	$R_p0.2$ (MPa)	R_m (MPa)	A50 (%)
BM	0.145	0.76	0.51	0.40	0.36	0.27	0.15	0.11	0.10	0.07	0.01	553	658	22
09G2S	≤ 0.12	1.00	≤ 0.3	-	0.65	≤ 0.3	≤ 0.3	≤ 0.03	-	≤ 0.12	≤ 0.035	350	500	21

$R_p0.2$ yield strength, R_m ultimate tensile strength, A50 elongation

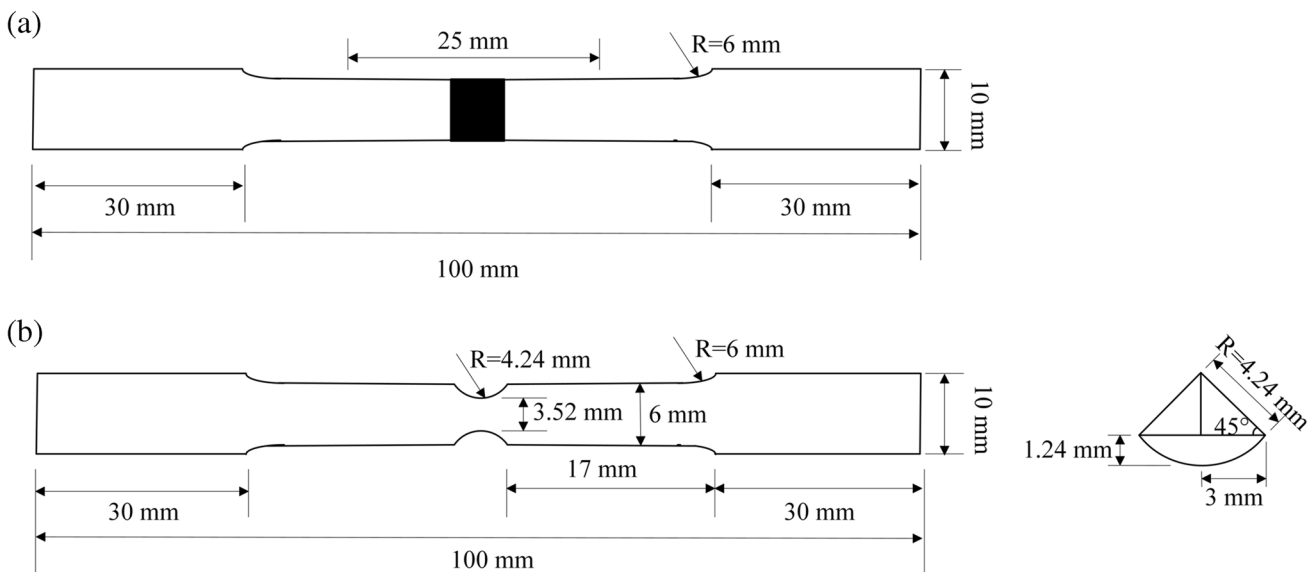


Fig. 2 The geometry of the welded samples for tensile shear tests **a** without a notch and **b** with a notch

3 Results and discussion

3.1 Geometric and mechanical features

The macroscopic views of the welded samples are illustrated in Fig. 3. A couple of welds seem to have linear misalignment that is caused by the inaccurate assembly of the metal sheets during the GMAW process. The welded samples can be categorized into three groups based on their geometric features [17], namely, insufficient penetration with convex top reinforcement, full penetration, and insufficient penetration with concave top reinforcement. These three kinds of welded joints are produced by different welding heat inputs. They are produced by different levels of welding heat input from a small amount to an excessive amount. As shown in Fig. 3, all of these three kinds of weld beads were achieved in this investigation. A few geometric features of the weld bead were measured and obtained via the software of ImageJ. The geometric characteristics consist of top reinforcement width, top

reinforcement height, penetration depth, bottom reinforcement width, and bottom reinforcement height.

Figure 4 presents the influence of voltage on the weld bead profile. The weld beads are produced by three levels of voltage. It is plain that the top reinforcement width, bottom reinforcement width, and bottom reinforcement height rise while the voltage increases from 15 to 17 V. Nonetheless, the top reinforcement height initially declines with the voltage until getting to its valley point, and then, it faintly increases when the voltage continues to increase. Its final value is still lower than the original height. It is understood that the voltage is rather crucial, for it is proportional to the welding heat input. Figure 4d reveals that the voltage has a remarkable effect on the penetration depth that proportionally rises with the levels of voltage. However, the penetration depth initially increases, and then, it keeps a stable value of 3.0 mm. When the voltage is 15 V, the penetration depth is about 2.5 mm, which is inferior to the thickness of the welding plates. Therefore, the bottom reinforcement has not appeared. Both its width and height are zero. The penetration

Fig. 3 The geometry of the welds



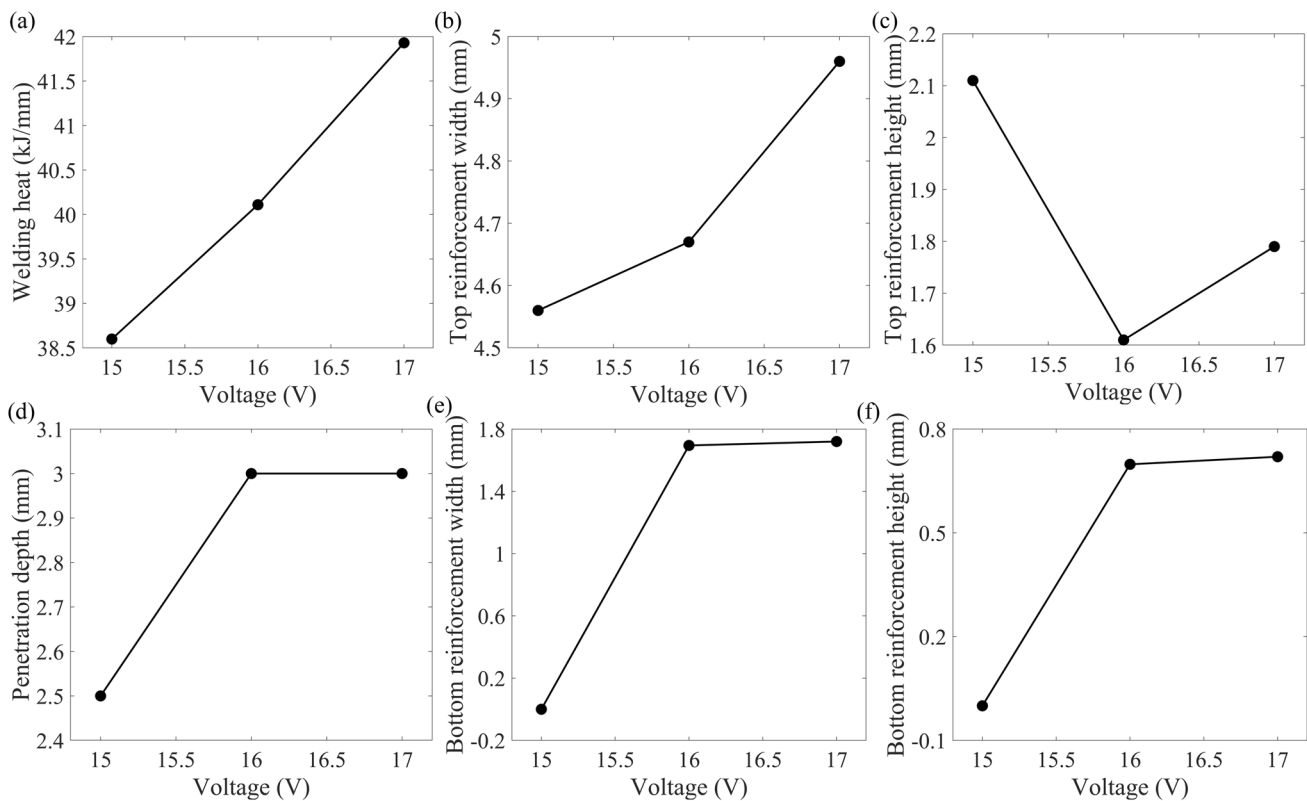


Fig. 4 The effect of the voltage on the geometric features of the weld bead (wire feed speed, 4.5 m/min; welding speed 45 cm/min)

depths of the weld beads with the voltage of 16 V and 17 V are 3 mm which equals the thickness of the BM, which indicates that the penetration depth gets to its peak due to the sufficient welding heat inputs under the current welding settings. The upper reinforcement width, bottom reinforcement width, and bottom reinforcement height rise as the voltage changes from 16 to 17 V, which is in keeping with the interpretations mentioned earlier. However, the upper reinforcement height of the weld bead produced by the voltage of 16 V is the smallest, which seems to be against the theory. This scenario may have resulted from laboratory sampling errors, for the differences in the welding heat input between the voltages of 16 V and 17 V are slight.

Figure 5 implies that the bottom reinforcement declines with the rise of the traveling speed of the welding electrode. The top reinforcement width reduces when the welding speed increases. The welding heat supplied to the per unit dimension of the weld bead decreases with the rise of the welding speed; therefore, the amount of the filler wire that is supposed to melt declines, bringing about a reduced weld width of the top reinforcement as well as the bottom reinforcement. Hence, the welding speed indicates an undesirable influence on these weld bead features. However, the upper reinforcement height stays minus as the welding speed is 25 cm/min, after which it increases with the welding speed

until reaching its peak value, whereas the penetration depth firstly rises with the welding speed and decreases subsequently. Actually, as the welding heat input exceeds a certain critical value, the melting speed of the BM is so rapid that the deposit amount of the filler wire is not able to fill all the room of the melting material of the BM. In these circumstances, portions of the top reinforcement will collapse into the weld pool leading to the deterioration of the dimensions of the top reinforcement. If the welding heat keeps on increasing and becomes too excessive, all the top reinforcement will be merged into the weld pool and it turns out to be flat even sunken. Meanwhile, the bottom reinforcement appears and develops due to the excessive melting metal from the filler wire and BM. That is why the top reinforcement height increases rather than decreases as the welding speed gets faster.

Wire feed speed is the quantity of melting filler wire supplied into the weld pool. The wire feed speed is usually considered to be connected with the welding current, determines the amount of metal deposit, and influences the reinforcement height and penetration length of the weld bead. In fact, the link governing the wire feed speed and welding current is almost linear. As for the constant voltage (CV) welding mode, the wire feed speed is directly connected to the level of the welding current moving across the welding

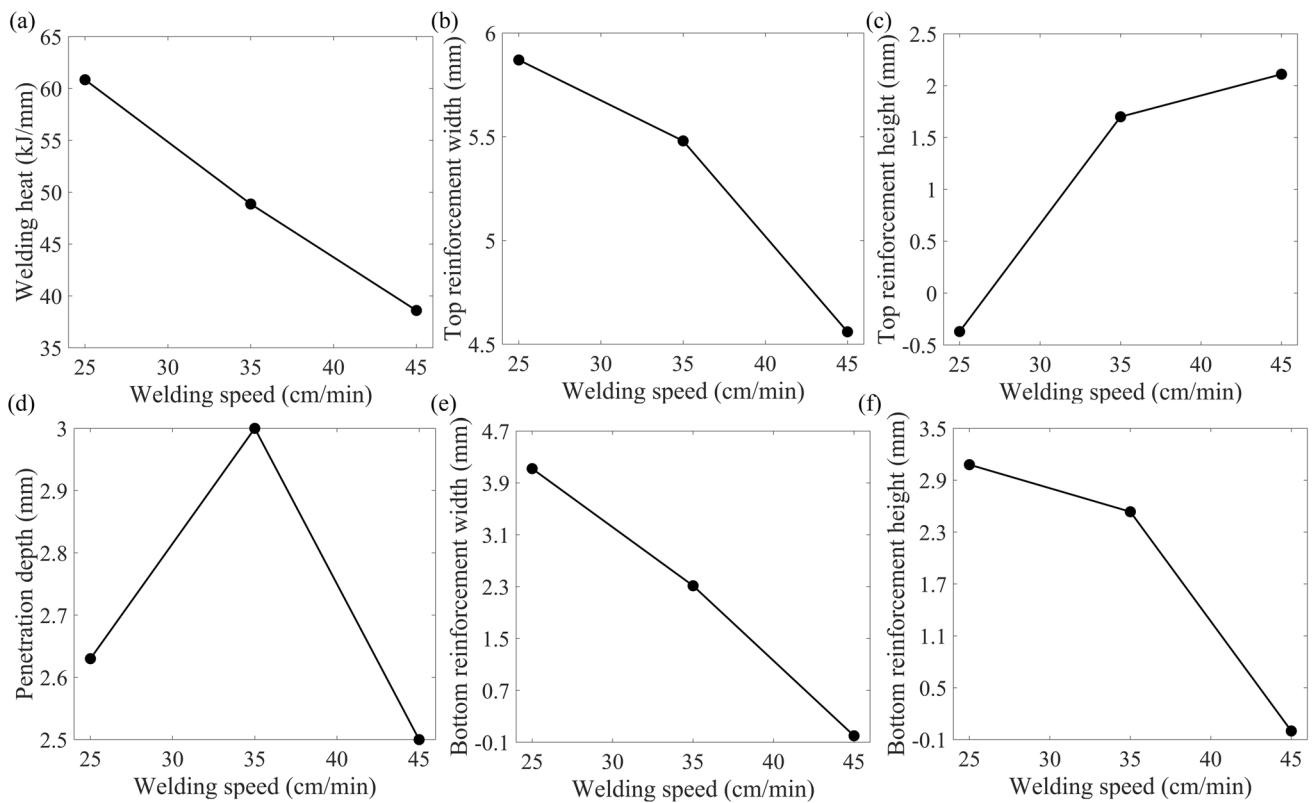


Fig. 5 The effect of the welding speed on the geometric features of the weld bead (voltage, 15 V; wire feed speed, 4.5 m/min)

arc. The power supply of the welding machine adapts and employs the suitable value of the welding current to melt the filler wire in keeping with the designated wire feed speed for welding operations in CV mode [18]. As a general rule, higher electromagnetic Lorentz force results in deepening the weld pool due to higher welding current, which leads to larger penetration depth. However, the penetration depth of the samples produced by different levels of the wire feed speed keeps a constant value of 3 mm which equals the thickness of the welding plates, as displayed in Fig. 6. At the same time, all the values of the bottom reinforcement height and width under various wire feed speeds are larger than zero. It indicates that all the welding heat inputs are high enough to melt sufficient metal and produce the bottom reinforcement. In point of fact, the welding heat remains at such a huge level that the melting rate of the BM is superior to that of the feeding wire. Hereafter, the height of the top reinforcement drops rather than increases.

3.2 Mechanical properties

The tensile tests were implemented on the welded samples without notch and their results were summarized. The displacement-load plots of the welded samples and BM are displayed in Fig. 7. Apparently, nearly all the welded joints

show identical results and fail at the BM. Even the samples do not have an excellent appearance. The failure is usually expected to start from the weak points of the weld. But the welds we got in this investigation seem to oppose this expectation and all of them break at the BM. It can be deduced from this fact that the welded joint is stronger than the BM. Hence, stress concentrates on the BM and causes it to yield. The possession of such a high tensile strength is owing to its microstructure in FZ. As it will be offered in Section 3.3, a large percentage of acicular ferrite (AF) and some grain boundary ferrites (GBF) are packed in FZ. Among them, AF has high mechanical strength and can bear larger loads than the microstructure in BM [19].

The tensile yield strength of the welded joint is around 596 MPa. Its mechanical performance is quite a resemblance to that of the BM. Bear in mind that the BM sheet is cut in such a path that is vertical to its rolling direction; thus, it has a fairly strong yield strength. Besides, the weld metal displays superior mechanical strength to the BM, because the filler wire employed in this study has a rather close chemical composition to the BM (Table 1). The welded joints produced by the BM and the filler wire with a similar chemical composition attain higher tensile strength than the BM. Unfortunately, it is improbable to evaluate the tensile strength of the welded joints under different welding

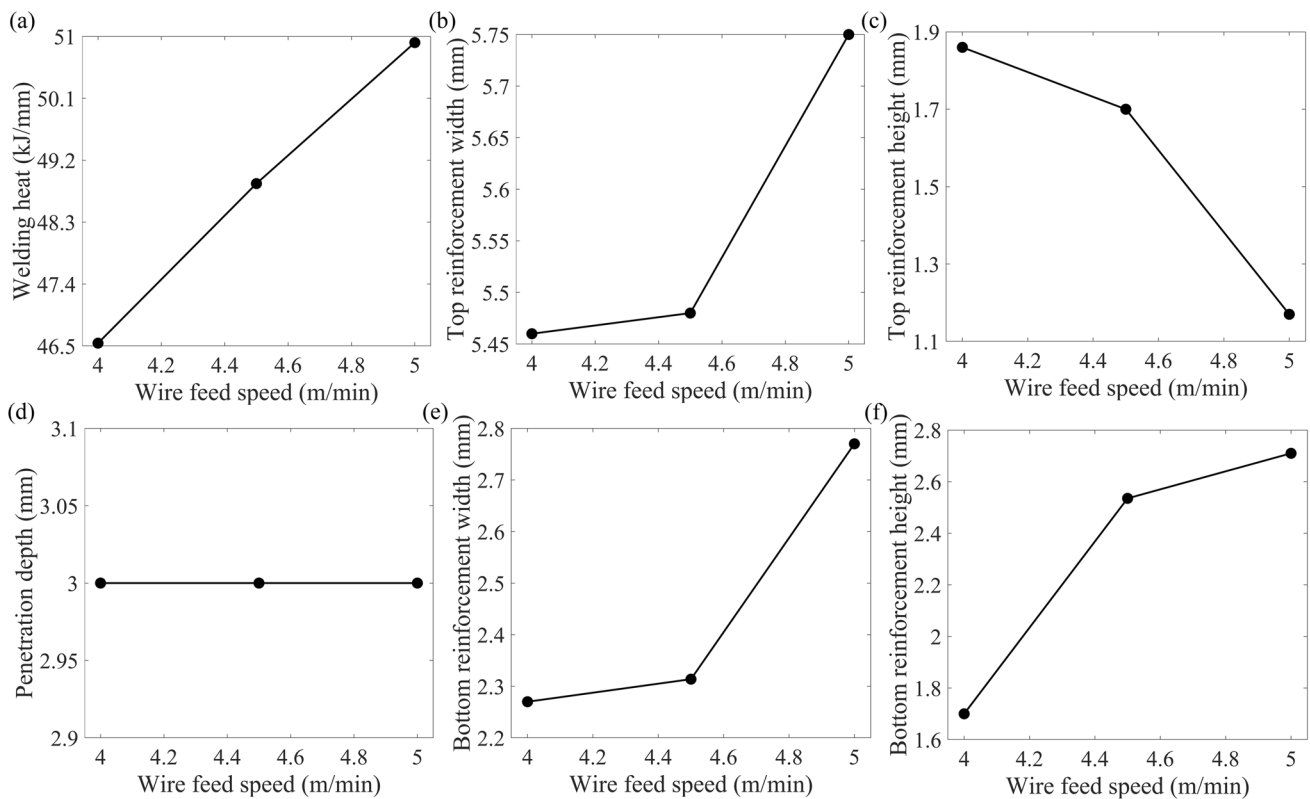


Fig. 6 The effect of the wire feed speed upon the geometric features of the weld bead (voltage, 15 V; welding speed, 35 cm/min)

parameters, as all the test results are identical to the tensile properties of the BM instead of their own tensile properties. That is why it is very necessary to make a notch at the

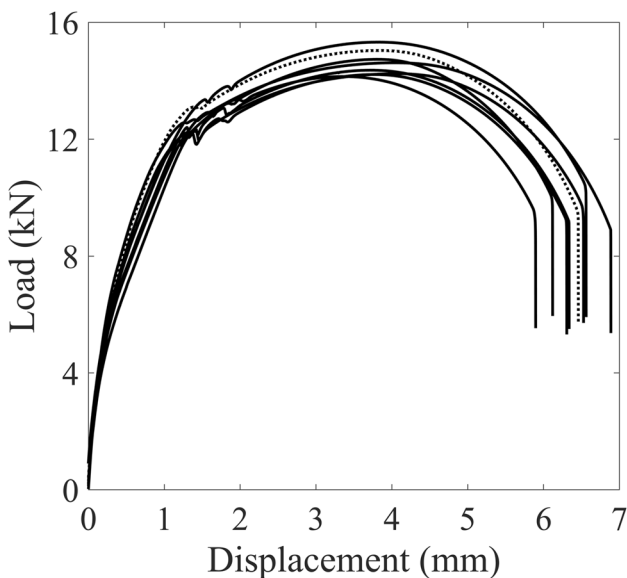


Fig. 7 The load–displacement plots of the BM and welded joints (solid line-welded joints without linear misalignment, dashed line-welded joints with linear misalignment)

weld to make its geometry change abruptly so that a stress concentration point is formed at the weld metal throughout the tensile process. Thus, the failure position that happens in the welded specimens is ensured.

Figure 8 displays the influences and effects of the welding speed on the peak load, maximum displacement, and failure energy of the mechanical properties. The range of the peak load is between 7.00 and 10.62 kN, and the upper and lower levels of the maximum displacement are individually 0.92 mm and 2.07 mm, whereas the failure energy ranges from 4.42 to 15.75 J. It can be grasped from Fig. 8 that the peak load rises as the welding speed increases until reaching its maximum point. Therefore, the welding speed displays a hefty influence on the mechanical attributes of the weld bead. Similarly, it can be perceived from Fig. 8a that the maximum displacement increases with the welding speed, and then, it tends to decline as the same factor further increases. The reason is that the welding heat input supplied to the weld zone declines while the welding speed increases, leading to a smaller size of the FZ. Actually, the welding heat input is oppositely proportional to the welding speed. In this case, increasing the welding speed means lessening the welding heat input. Therefore, higher welding speed gives rise to the reduction of the penetration depth and less time for accumulating the welding heat flow. Instead, slower

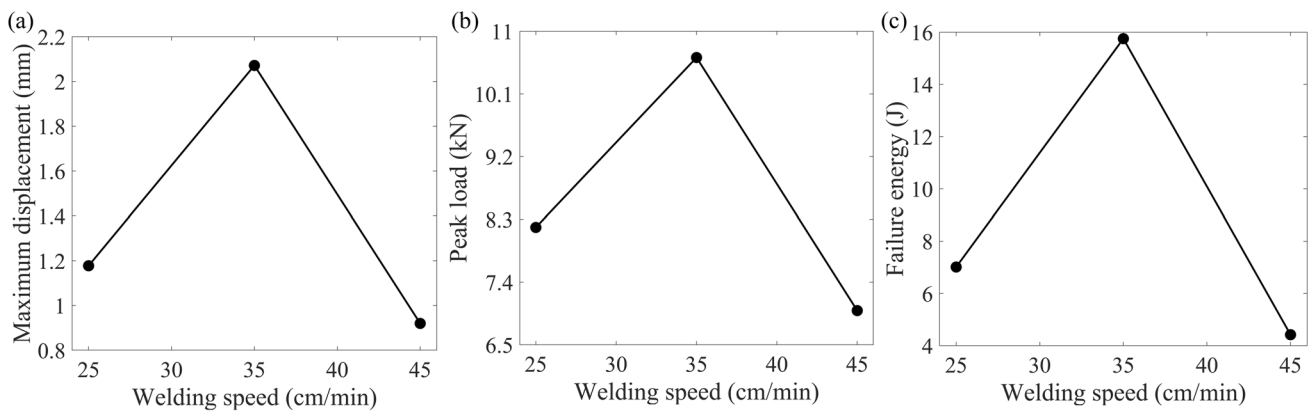


Fig. 8 The effect of the welding speed upon the mechanical attributes of the welded joints (voltage, 15 V; wire feed speed 4.5 m/min)

welding speed implies higher welding heat input, which can guarantee a longer period for the weld pool to stay liquid. Subsequently, the increasing welding heat flows into the welding material, enlarges the FZ, and deepens the penetration. However, quite a low level of welding speed may cause the BM to be degraded under the effect of the extreme arc heat and lead to over-deposition [20]. Thus, an appropriate and medium level of welding speed should be employed to modify the mechanical attributes of the weld bead.

The influences of the voltage upon the mechanical attributes of the weld bead are revealed in Fig. 9. The welding voltage is the potential difference between the surface of the weld pool and the electrode tip. The peak load of the welded joints increases with the voltage ranging from 15 to 17 V as the remaining welding parameters are set constant. All the other mechanical attributes of the welded joints firstly increase with the voltage until getting to peaks and afterwards decrease with the further increase of the same factor. The welding voltage determines the arc length, which sequentially controls the shape and profile of the weld bead. Under the welding conditions of setting other welding

parameters constant, boosting the voltage will give rise to a wider and flatter weld bead and reduce the porosities simultaneously [21]. As a general rule, the melting speed of the filler wire declines with the decrease of the welding heat input. The volume of the deposition caused by the melting filler wire is in straight proportion to the welding heat input. Hence, it increases with the voltage. An extremely high voltage is prone to yield a hat-shaped weld that presents a concave profile. This sort of weld bead has a tendency to contain several welding defects, for example, crack, bite, and undercut at the rim of the weld. Conversely, too low a voltage may produce high and narrow weld beads that are undesirable. In this case, the voltage with the value of 16 V is preferable.

As the CV welding mode is employed in this work, the welding machine is able to adjust the suitable welding current to melt the filler wire relying on the pre-set value of wire feed speed. The influence of the electromagnetic Lorentz force becomes more significant with the rise of the welding current, which in turn causes deeper penetration. The influence of the wire feed speed upon the mechanical strength

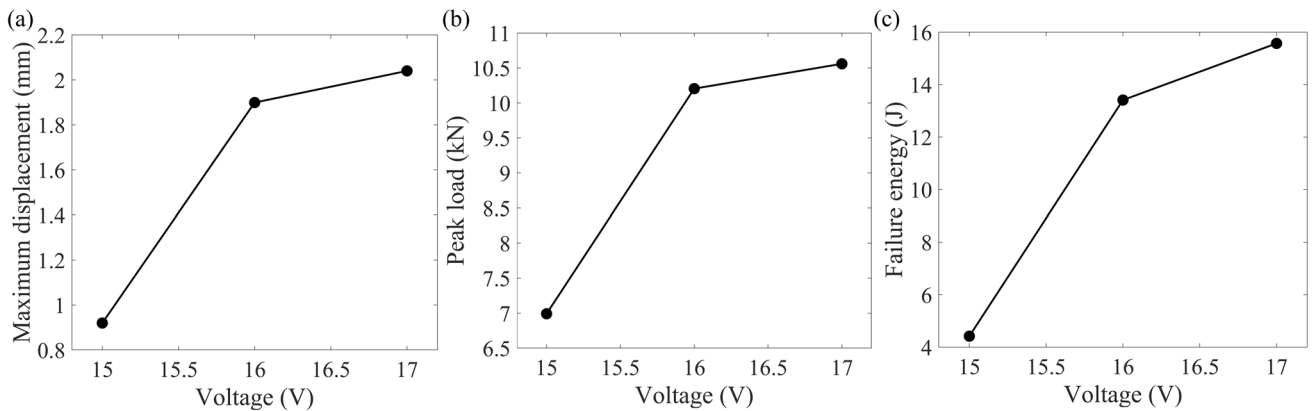


Fig. 9 The effect of the voltage on the mechanical attributes of the welded joints (wire feed speed, 4.5 m/min; welding speed, 45 cm/min)

of the weld bead is presented in Fig. 10, where it can be grasped that the medium level of the wire feed speed produces the weld with the maximum mechanical performance. The welding heat input increases as a larger wire feed speed is employed. For instance, a wire feed speed of 5 m/min will yield roughly 10% higher welding heat input delivered to the weld zone than that is produced by a wire feed speed of 4 m/min with other welding parameters unchanged. The quantity of metal deposited in the weld pool is straight proportional to the welding heat input. If a huge heat input is employed during welding, more filler wires will melt. Thus, the deposition area extends with the rising of the welding current. However, the mechanical attributes of the welded

joints produced by the wire feed speed of 5 m/min are inferior to that of the medium-leveled wire feed speed.

3.3 Microstructure

The microstructure of the as-received BM is demonstrated in Fig. 11a. The BM comprises ferrite and pearlite. The white part in Fig. 11a is pearlite while the dark portion is ferrite. During the GMAW process, the maximum temperatures at different places of the weld zone are different. Based on the difference in the peak temperature, several areas without strict lines can be classified in the HAZ. In general, the welded joints are basically composed of the FZ, WI,

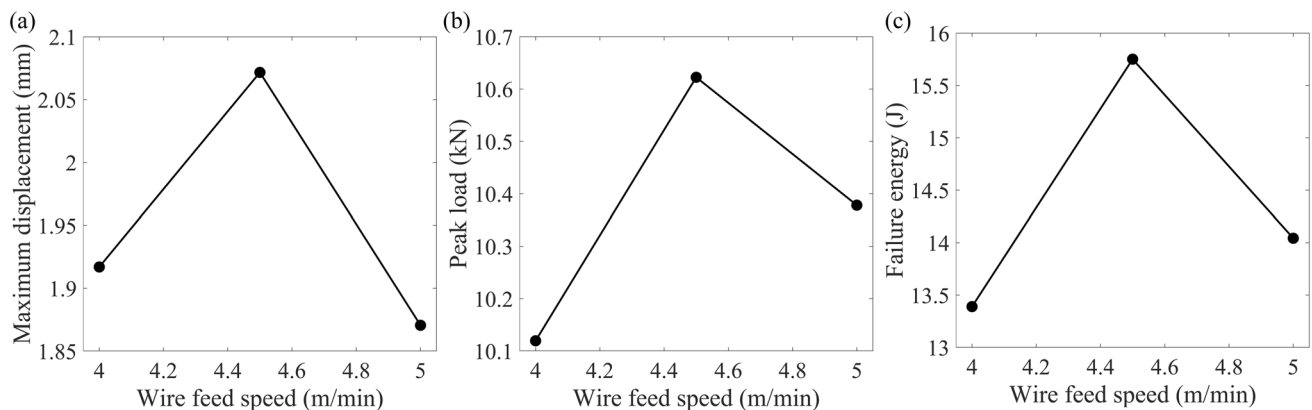


Fig. 10 The influence of the wire feed speed upon the mechanical attributes of the welded joints (voltage, 15 V; welding speed, 35 cm/min)

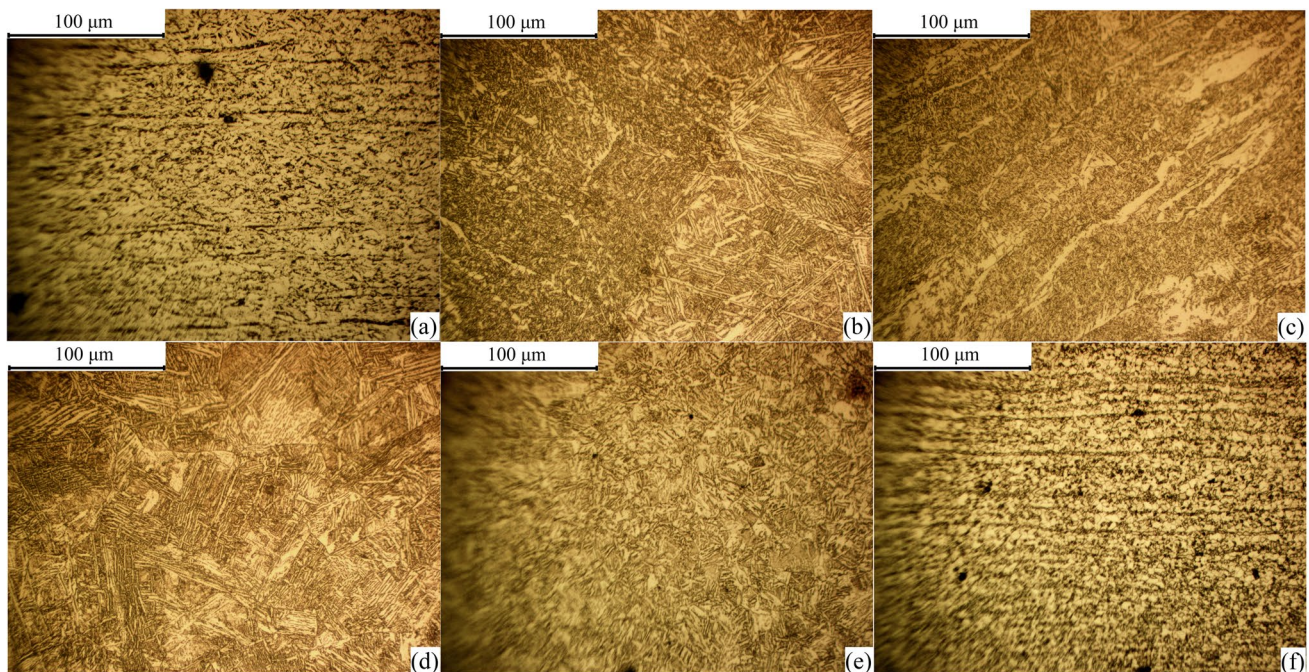


Fig. 11 The microstructure of the welded joints obtained by the optical microscope. **a** BM; **b** WI; **c** FZ; **d** CGHAZ; **e** FCHAZ; **f** ICHAZ

coarse-grained heat-affected zone (CGHAZ), fine-grained heat-affected zone (FGHAZ), inter-critical grain heat-affected zone (ICHAZ), and BM from the inner to outer.

FZ has a columnar structure, and the dendrites are mainly placed facing maximum heat transfer, that is, perpendicular to the WI and toward the weld center. The weld center itself is formed by isometric dendrites, while the FZ near the weld has a honeycomb structure. The growth rate is relatively low, and the temperature gradient is huge. The isometric dendrite area is suppressed, forming columnar dendrites in the center of FZ. AF, polygonal GBF, Widmanstätten ferrite, and block ferrite (BF) are noticed in the FZ, as revealed in Figs. 11c and 12. This is caused by the steep temperature gradient in the FZ, which is in the state of liquid in the welding process. The dendrites develop perpendicular to the WI and intersect in the heart of the melted weld pool. Solidification of the molten material in the FZ is a dynamic process of crystal epitaxial development, temperature gradient, and crystal growth rate. In terms of the welding solidification procedures, the crucial elements affecting microstructure include the temperature gradient, growth rate, undercooling degree, and alloy structure in the weld pool. All these factors essentially vary with different fusion locations, welding process parameters, and welding settings. The fusion line that separates the FZ and CGHAZ is detected in Fig. 11b.

A similar way to FZ occurs in the microstructure transformation in the HAZ, but it produces different microstructures. CGHAZ refers to a relatively narrow area close to the WI. The peak temperature in CGHAZ ranges between Ac_3 ($857\text{ }^\circ\text{C}$) [22] and the melting point of BM (about $1500\text{ }^\circ\text{C}$). Therefore, complete austenization occurs. In addition, the temperature is also greater than the temperature when the austenite grains get coarsening. Attributable to the high temperature, most of the precipitates (carbides, nitrides, and carbonitrides) dissolve, resulting in thicker grains than the BM. Therefore, the austenite grains develop and eventually become larger in size. As can be detected from Figs. 11d and 13, lath bainite (LB), lath martensite (LM), granular bainite (GB), blocky M-A constituent (island of the second phase, composed of martensite and residual austenite), Widmanstätten ferrite, and prior austenite grain boundaries are the leading structures of CGHAZ [23–25].

The next area, FGHAZ, is the most extensive fine-grained part of the HAZ, which represents the normalized area. The temperature of FGHAZ is between Ac_3 and the austenite grain coarsening point (about $1200\text{ }^\circ\text{C}$) [26]. Therefore, small-size austenite will appear under the influence of welding heat. After that, due to the cooling speed, in FGHAZ, PF, bainite, and pearlite with quite fine grains are packed (Figs. 11e and 14a).

Fig. 12 The microstructure of FZ obtained by the SEM

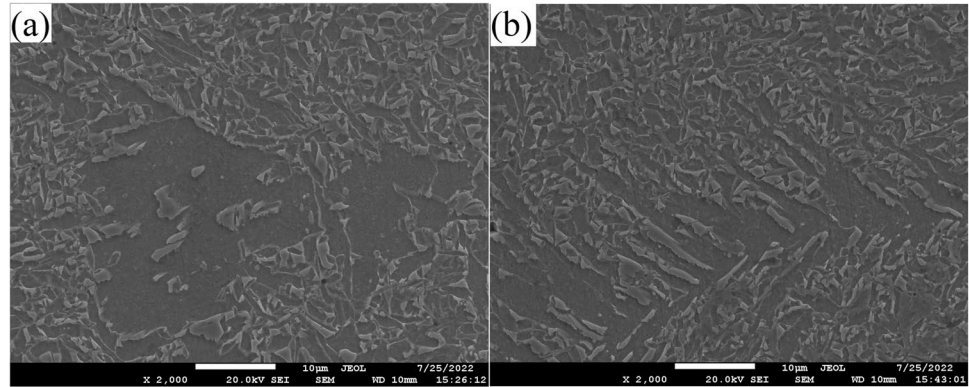


Fig. 13 The microstructure of CGHAZ obtained by the SEM

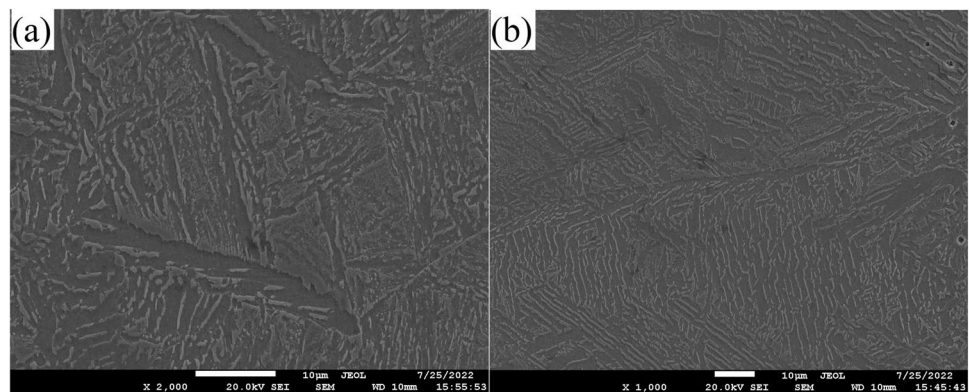
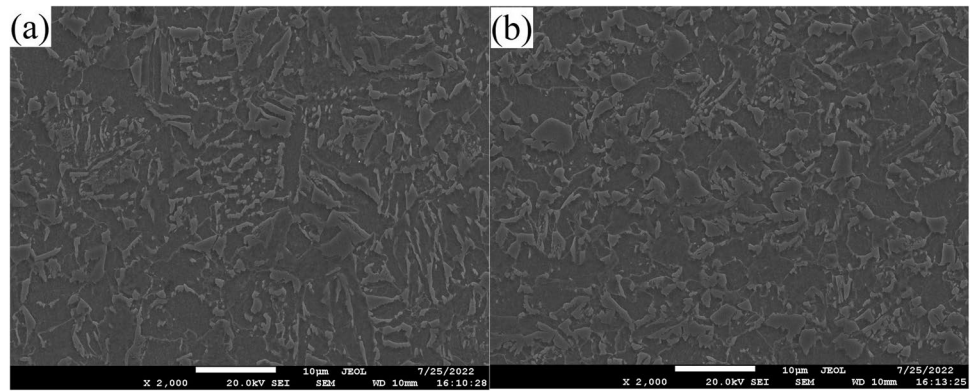


Fig. 14 The microstructure of **a** FGHAZ and **b** ICHAZ obtained by the SEM



The third region is ICHAZ, which represents the recrystallized region, in which the partially transformed pearlite and ferrite are comparable with the BM. ICHAZ is a narrow area near BM, with peak temperatures within the range of A_{c1} (731 °C) [22] and A_{c3} (857 °C). Therefore, part of the BM is austenitized. In the short cooling stage, the austenite is transformed into pearlite. Due to the different maximum temperatures in different locations, the closer it is to the weld center, the higher the temperature will be. It can be perceived that the proportion of pearlite formed declines with the distance from the weld centerline, as revealed in Figs. 11f and 14b.

Different levels of voltage alter the microstructure because the effect of weld size and cooling speed is different as the welding heat input is attained by changing the voltage. As previously mentioned, increasing the voltage increases the rate of metal melting, thereby increasing the HAZ geometry and grain coarsening. The initial austenite grain size in the FZ expands with the rise in the supplied welding heat. High welding heat input and lower cooling speed promote grain growth, as proved in Fig. 15.

Increasing the wire feed speed, thereby increasing the heat input, reducing the weld cooling rate, and extending the solidification time, can be expected to have a coarser phase of the

weld metal. At 5 m/min, the original austenite grain dimension of FZ is about 2 times of the corresponding grain size of 4 m/min, as shown in Fig. 16. This is to be anticipated, as increasing the wire feed speed (welding current) correspondingly increases the welding heat input, ending in a reduction in the cooling rate. Thus, during the austenite-ferrite transformation, the FZs take a long period at high temperatures, thereby coarsening the grains.

Figure 17 displays a typical optical micrograph of the FZ. It represents the different dimensions of the austenite grains formed by welding speeds of 25 cm/min, 35 cm/min, and 45 cm/min. Cautious visual examination exposed the prior austenite grains that stayed largest at the lowest welding speed (25 cm/min), which symbolized the highest heat input (60.84 kJ/mm) and the lowest cooling rate. In all cases, the prior austenite grain size was observed to decrease with increasing speed. This is reasonable since, at low welding speeds, the resulting high heat input produces large FZs that need a long period to solidify. Consequently, the weld is exposed to a high-temperature range for a long period, creating huge prior austenite grains. As the heat input decreases and the cooling rate increases, the duration remaining at a high temperature after the weld solidifies will decrease, thereby hindering grain growth.

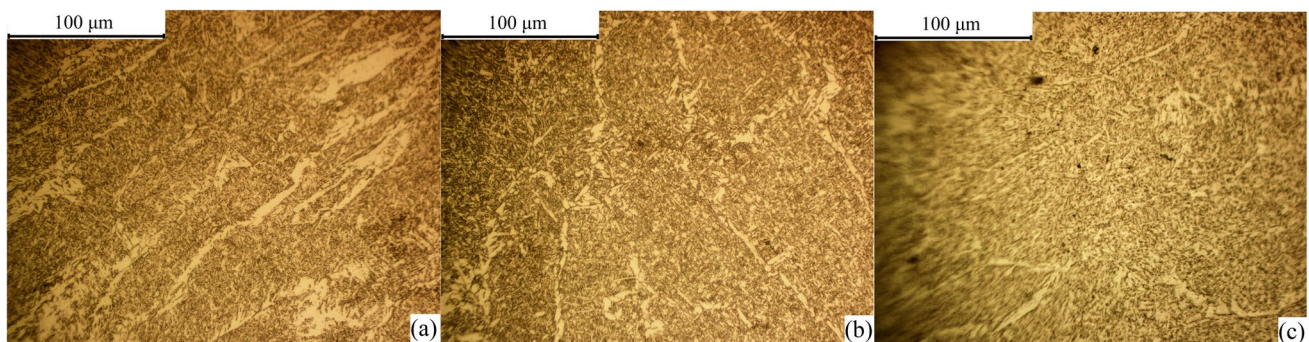


Fig. 15 The microstructure of FZ with different voltages. **a** 15 V; **b** 16 V; **c** 17 V

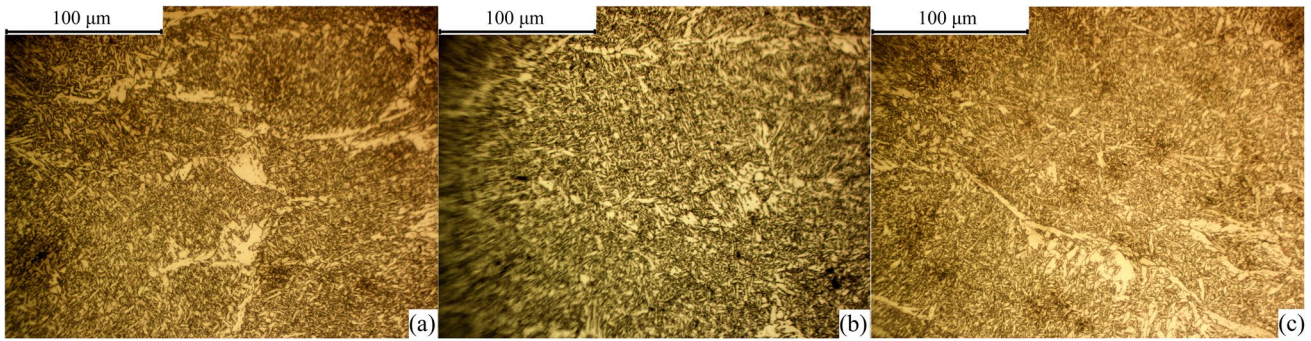


Fig. 16 The microstructure of FZ with different wire feed speeds. **a** 4 m/min; **b** 4.5 m/min; **c** 5 m/min

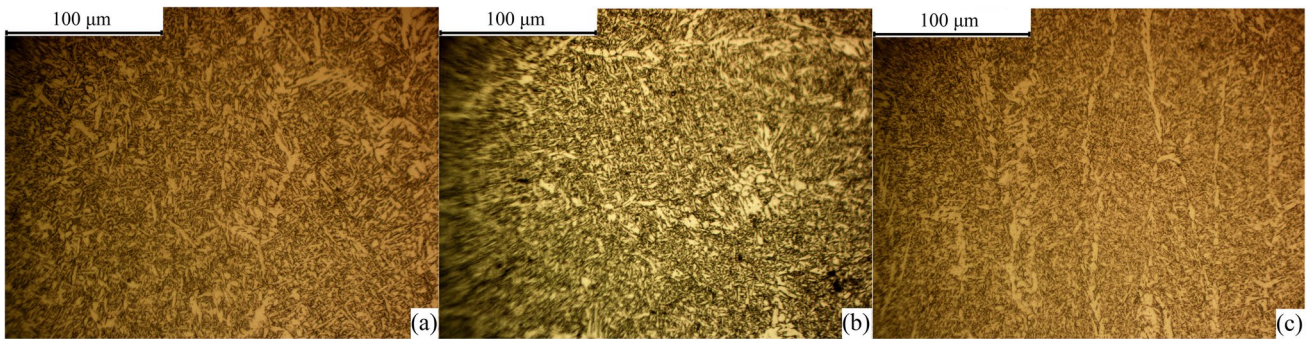


Fig. 17 The microstructure of FZ with different welding speeds. **a** 25 cm/min; **b** 35 cm/min; **c** 45 cm/min

3.4 Microhardness

The hardness profile of the welded joint is presented in Fig. 18, which expresses changes in hardness across the weld section. As can be perceived from this figure, the hardness of the BM is the lowest, while the hardness is the highest at the WI. The average hardness of FZ is greater than that of FGHAZ. Thus, the order of increasing hardness distribution with respect to the hardness of the weld zone is as follows: WI > CGHAZ > FZ > FGHAZ > BM.

Generally speaking, the overall hardness of a metal is determined by the hardness of the various phases it has. Hence, it is very vital to explore the relationship between the hardness and microstructure in different areas of the weld. The WI and CGHAZ are the regions with the highest temperature gradients, so more hardened microstructures can be expected there to increase their hardness levels.

The high hardness of the WI or CGHAZ can be clarified by the transformation and changes in the microstructure of the welds during the GMAW process. The microstructure of CGHAZ can be associated with two stages of the transition, namely, (i) the production of austenite in CGHAZ has sufficient time to grow, leading to a rather coarsen size. (ii) Because of the rapid cooling speed of the CGHAZ as well as the carbon percentage of the BM, the large-sized austenite transfers to pearlite and bainite. The more adjacent the CGHAZ to the WI, the quicker the cooling

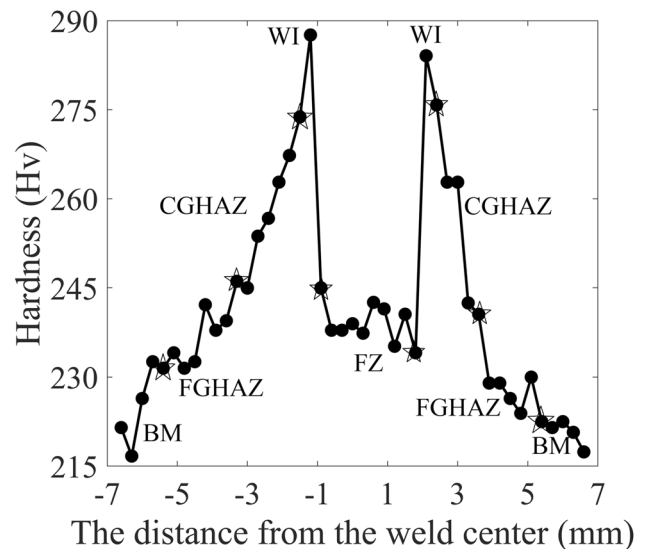


Fig. 18 A typical microhardness profile of the welded joint produced by the voltage of 15 V, wire feed speed of 4.5 m/min, and welding speed of 45 cm/min

speed and the larger the percentage of harder microstructure (bainite) will be produced. In such a case, it is anticipated that the WI and CGHAZ have the highest hardness.

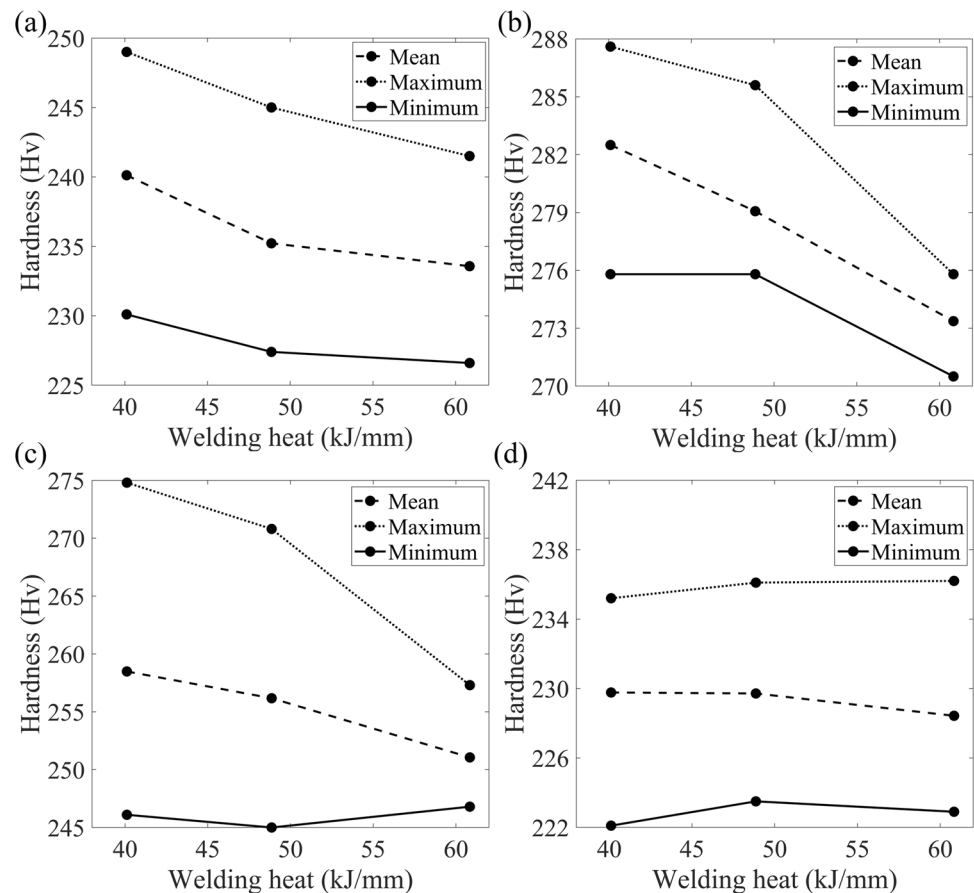
The appearance of AF contributes to the high hardness of the FZ. The AF is shaped like a needle and characterized by a disordered arrangement of fine-grained ferrite sheets with different orientations separated by high-angle grain boundaries [27]. This resulting microstructure is better than bainite or Widmanstatten ferrite which tends to form parallel plates in the same direction [27]. Therefore, the microstructure of AF can potentially have both high strength and high toughness. Consequently, the hardness of the FZ is also quite high.

Compared with the BM, the phase in FGHAZ is identical to the phase in the BM, excluding the fact that the grain width of the phase in FGHAZ is inferior to the phase in the BM. According to the Hall–Petch equation, the yield strength increases when the grain size decreases. Thus, the yield strength of FGHAZ is superior to that of the BM. Accordingly, the hardness of FGHAZ is greater than that of the BM.

Figure 19 displays the influence of heat input upon the hardness of the welds. There are 3 curves in each graph, maximum hardness, minimum hardness, and average hardness. Figure 19 shows that the hardness of FZ, WI, and CGHAZ decreases significantly with increasing heat input, while the hardness of BM and FGHAZ has few connections

with the welding heat input. For example, when the heat input increases from 40.11 to 60.84 kJ/mm, the average hardness of FZ decreases from 240 to 234 Hv. The hardness of CGHAZ decreases from 259 to 251 Hv. This might be attributable to the reduction of thermal gradient due to high welding heat input and the improvement of a coarse grain structure and the soft phase ratio due to a low cooling rate. As the welding heat increases, the microhardness distribution of FZ gradually becomes uniform. When the welding heat input is kept at 60.87 kJ/mm, the difference between the maximum and minimum hardness is small due to the large current, high heat generation, and slow cooling rate. Given enough time to complete the phase transformation, a uniform FZ microstructure can be obtained, resulting in uniform microhardness. Figure 19 shows that the hardness levels of the BM and FGHAZ will not change much with the heat input, since the phases in these areas are ferrite and pearlite. The ratio of ferrite and pearlite in these areas will not change, since these proportions are determined by the chemical composition of the BM, especially the carbon content. Because the composition of these sections did not change, the strength of the BM and FGHAZ did not practically change during the GMAW process.

Fig. 19 The effects of welding heat inputs upon the microhardness distribution in **a** FZ, **b** WI, **c** CGHAZ, and **d** FGHAZ



3.5 Optimization of the welding parameters

3.5.1 Arranging additional welding experiments

To build the models quantifying the relationships between the welding process parameters and welding quality indexes, additional welding experiments are intended to be carried out. The selected variable parameters consisted of welding speed, wire feed speed, and voltage. In order to increase the reliability and usability of test results, experiments were organized based on the design of experiment (DOE) method. Compared with other experimental design methods, the Box-Behnken design (BBD) is considered suitable for a limited number of samples. A 95% default confidence interval is calculated based on experimental results of BBD. In this investigation, the BBD is finally selected, and the values of the welding process parameters for different levels are shown in Table 2. Table 3 illustrates the experimental results.

Table 2 Welding process parameters at different levels

Symbol	Process parameter	Unit	Level-1	Level 0	Level+1
A	Voltage	V	15	16	17
B	Wire feed speed	m/min	4	4.5	5
C	Welding speed	cm/min	25	35	45

Table 3 Experimental results based on BBD design

No	Voltage	Wire feed speed	Welding speed	Failure energy	The depth of penetration and bottom reinforcement	Standard deviation of failure energy
	V	m/min	cm/min	J	mm	J
1	15	4	35	12.21	4.7	2.05
2	17	4	35	12.83	3.93	0.94
3	15	5	35	12.88	5.71	2.23
4	17	5	35	12.83	4.37	0.51
5	15	4.5	25	14.13	5.71	6.18
6	17	4.5	25	14.05	6.37	0.83
7	15	4.5	45	4.7	2.52	0.55
8	17	4.5	45	15.57	3.72	2.96
9	16	4	25	12.86	6.41	3.55
10	16	5	25	16.71	6.92	5.12
11	16	4	45	8.51	2.34	2.7
12	16	5	45	13.36	4.7	3.75
13	16	4.5	35	14.18	4.7	0.68
14	16	4.5	35	14.24	6.48	1.11
15	16	4.5	35	13.29	5.38	0.68
16	16	4.5	35	13.97	3.71	0.62
17	16	4.5	35	13.51	5.25	1.19

3.5.2 Regression analysis

Nonlinear polynomial regression is a kind of statistical and mathematical method quantifying the relationships between the responses of interest and process parameters, which is adequate and reliable for modeling and analyzing practical production problems.

Generally, the errors of the continuous variables x_1, x_2, \dots, x_n are supposed to be too small to be ignored. The mapping relationship between the variable y and the independent variables can be expressed as [28]

$$y = f(x_1, x_2, \dots, x_n) + \varepsilon \tag{1}$$

where ε is the model error and includes measurement error as well as other variabilities. It is essential and needed to precisely estimate the mathematical model for the relationship between the dependent variable $f(x_1, x_2, \dots, x_n)$ and the independent variables x_1, x_2, \dots, x_n . In this study, $f(x_1, x_2, \dots, x_n)$ is a function of the welding parameters such as voltage (A), wire feed speed (B), and welding speed (C), which quantifies the welding quality of welded weathering steel A606 type IV. In general, a group of polynomial models is employed as follows:

$$f(x_1, x_2, \dots, x_n) = a_0 + \sum_{i=1}^n a_i x_i + \sum_{i=1}^n a_{ii} x_i^2 + \sum_{j \neq i}^n a_{ij} x_i x_j + \dots + \varepsilon \tag{2}$$

where ε is the model error. In addition, a_0 is the average of the responses, and a_i, a_{ij} , and a_{ii} are regression coefficients

that depend on respective linear, interaction, and squared terms of factors, which are obtained from the experimental data using the least square regression method.

The Design Expert Software was used to determine the regression coefficients and analysis of variance (ANOVA) with all the welding parameters, and their respective values were also performed, as listed in Tables 4, 5, and 6. In this study, the significant factors are judged by their P values. If its P value is larger than 0.1, it will be insignificant. The item with a P value less than 0.05 indicates it is quite significant. The lack of fit P value should be larger than 0.1, which indicates that the lack of fit is insignificant relative to the pure error. There is a chance with such a value that a lack of fit P value this large may occur due to noise. Non-significant lack of fit is satisfying; we want the model to fit. The fitting degree of the polynomial regression model was also examined by the determination coefficient. The coefficient of determination R^2 is always between 0 and 1, and its value indicates the capability of the model. With regard to a good statistical model, the R^2 value should be close to 1.0. The adjusted R^2 value reconfigures the fitting formula with significant terms. The value of the adjusted R^2 should also be large enough to support the high significance of the model. The predicted R^2 indicates the capability of the model in predicting completely new experimental data. Its value should be in reasonable agreement with the adjusted R^2 and the difference between them should be within 0.2. Adeq precision means the signal-to-noise ratio. A ratio greater than 4 is desirable, which indicates this model is able to navigate the design space. The results in Tables 4, 5, and 6 indicate the established models are significant since their P values are much less than 0.05. Besides, their

Table 4 ANOVA test results for the failure energy (E)

Source	Sum of squares	df	Mean square	F -value	P value
Model	115.79	9	12.87	90.73	<0.0001
A	0.08	1	0.08	0.57	0.4738
B	0.11	1	0.11	0.79	0.4032
C	30.46	1	30.46	214.81	<0.0001
AC	29.98	1	29.98	211.40	<0.0001
BC	0.25	1	0.25	1.76	0.2259
A^2	3.89	1	3.89	27.42	0.0012
C^2	2.62	1	2.62	18.45	0.0036
AC^2	13.06	1	13.06	92.08	<0.0001
BC^2	8.06	1	8.06	56.84	0.0001
Residual	0.99	7	0.14		
Lack of fit	0.29	3	0.10	0.55	0.6763
Pure error	0.70	4	0.18		

standard deviation=0.38; $R^2=0.992$; mean=12.93; adjusted $R^2=0.981$; C.V. (%)=2.91; predicted $R^2=0.955$; press=5.24; Adeq precision=42.32

Table 5 ANOVA test results for the depth of penetration and bottom reinforcement (H)

Source	Sum of squares	df	Mean square	F -value	P value
Model	20.72	2	10.36	17.44	0.000
B	2.33	1	2.33	3.93	0.068
C	18.39	1	18.39	30.96	0.000
Residual	8.32	14	0.59		
Lack of fit	4.22	10	0.42	0.41	0.884
Pure error	4.10	4	1.02		

standard deviation=0.77; $R^2=0.714$; mean=4.88; adjusted $R^2=0.673$; C.V. (%)=15.80; predicted $R^2=0.602$; press=11.56; Adeq precision=12.70

determination coefficients are also large enough. The model for the failure energy has the determination coefficients of 0.992, 0.981, and 0.955; while the values of the model for the depth of penetration and bottom reinforcement are 0.714, 0.673, and 0.602. The values of 0.957, 0.932, and 0.851 for the third model are also very close enough to each other. All the results indicate that the developed models have the capabilities to navigate the variables.

By analyzing all kinds of influencing factors and abandoning the nonsignificant factors, the regression coefficients are decided, and simple fitting formulas are presented as follows:

$$E = -799.44 + 52.57 \times A + 47.77 \times B + 37.01 \times C - 1.51 \times AC - 2.76 \times BC - 0.96 \times A^2 - 0.60 \times C^2 + 0.03 \times AC^2 + 0.04 \times BC^2 \quad (3)$$

$$H = 5.32 + 1.08 \times B - 0.15 \times C \quad (4)$$

$$\sigma = 214.51 - 7.51 \times A - 29.94 \times B - 4.61 \times C + 0.19 \times AC + 3.39 \times B^2 + 0.02 \times C^2 \quad (5)$$

Table 6 ANOVA test results for the standard deviation of failure energy (σ)

Source	Sum of squares	df	Mean square	F -value	P value
Model	45.59	6	7.60	37.31	<0.0001
A	4.16	1	4.16	20.44	0.0011
B	0.70	1	0.70	3.45	0.0930
C	4.09	1	4.09	20.08	0.0012
AC	15.05	1	15.05	73.92	<0.0001
B^2	3.04	1	3.04	14.91	0.0032
C^2	17.67	1	17.67	86.76	<0.0001
Residual	2.04	10	0.20		
Lack of fit	1.74	6	0.29	3.96	0.1021
Pure error	0.29	4	0.07		
Cor total	47.63	16			

standard deviation=0.45; $R^2=0.957$; mean=12.93; adjusted $R^2=0.932$; C.V. (%)=21.52; predicted $R^2=0.851$; press=7.07; Adeq precision=19.31

where

$$\begin{aligned} 15V &\leq A \leq 17V \\ 4\text{m/min} &\leq B \leq 5\text{m/min} \\ 25\text{cm/min} &\leq C \leq 45\text{cm/min} \end{aligned} \tag{6}$$

The relative importance of the welding parameters can be obtained by their *P* values. The welding speed has the most profound effect on the failure energy since its *P* value is the least. The wire feed speed and voltage affect the failure energy via the interaction effects. The declining order of the significance of the welding parameters for the standard deviation is voltage, welding speed, and wire feed speed.

3.5.3 Determine the optimum welding parameters

One of the basic aims of this study was to obtain the optimal parameters for the welding quality. The purpose is to calculate the optimal voltage, wire feed speed, and welding speed for maximum absorbed energy, the depth of the penetration and bottom reinforcement of 3 mm, and the minimum standard derivation of absorbed energy by the desirability method. The desirability equations for calculating the corresponding failure energy $d_1(A, B, C)$, depth of penetration and bottom reinforcement $d_2(A, B, C)$, and standard deviation of failure energy $d_3(A, B, C)$ are as follows:

$$d_1(A, B, C) = \frac{E(A, B, C) - 4.70}{16.71 - 4.70} \tag{7}$$

$$d_2(A, B, C) = \begin{cases} \frac{H(A,B,C)-2.34}{3-2.34} & 2.34 \leq H(A,B,C) \leq 3 \\ \frac{H(A,B,C)-6.92}{3-6.92} & 3 < H(A,B,C) \leq 6.92 \end{cases} \tag{8}$$

$$d_3(A, B, C) = \frac{\sigma(A, B, C) - 6.18}{0.51 - 6.18} \tag{9}$$

In this case, the overall desirability function is defined as follows:

$$d = (d_1^3 \times d_2^3 \times d_3^3)^{\frac{1}{3+3+3}} \tag{10}$$

Table 7 The settings of the optimization

Name	Goal	Lower	Upper	Lower	Upper	Importance
A	Is in range	15	17	1	1	3
B	Is in range	4	5	1	1	3
C	Is in range	25	45	1	1	3
E	Maximize	4.7	16.71	1	1	3
H	Is target=3	2.34	6.92	1	1	3
σ	Minimum	0.51	6.18	1	1	3

The importance of each desirability equation is determined according to its importance [29]. In this investigation, the failure energy, the depth of penetration and bottom reinforcement, and the standard derivation of absorbed energy are equally important, and their weight is equal to 3, which is consistent with the expression (10). The ranges of operating conditions (voltage, wire feed speed, welding speed) and the goal for optimization are defined in Table 7. The optimum welding parameters were determined according to Eq. (10) and described in Table 8. Based on the results, *A* = 16.91 V, *B* = 4.29 m/min, and *C* = 40.11 cm/min should be chosen.

3.5.4 Verification test and comparison of weld geometry and mechanical properties of welded joints before and after optimization

Changes in the physical and metallurgical properties of welded joints after optimization should be investigated. The welding parameters were selected according to Table 8, and the values of voltage 17 V, wire feed speed 4.3 m/min, and welding speed 40 cm/min were selected for the welding operation. The weld geometry and strength of the welded joints have a significant impact on mechanical weld quality indicators. The weld geometry and mechanical properties of the welds before and after optimization were obtained and compared.

Figure 20 shows the load–displacement diagram of the optimized welded joints obtained after the tensile shear test. Typically, the maximum displacement, failure energy, and peak load are calculated from each curve to characterize the mechanical properties of the welded joint. It can be seen that the average peak load (*P*), maximum

Table 8 The optimum technological parameters achieved by the desirability approach

No	Voltage	Wire feed speed	Welding speed	Desirability
1	16.91	4.29	40.11	0.793
2	16.91	4.29	40.13	0.793
3	16.90	4.29	40.12	0.793
4	17.00	4.30	40.30	0.792

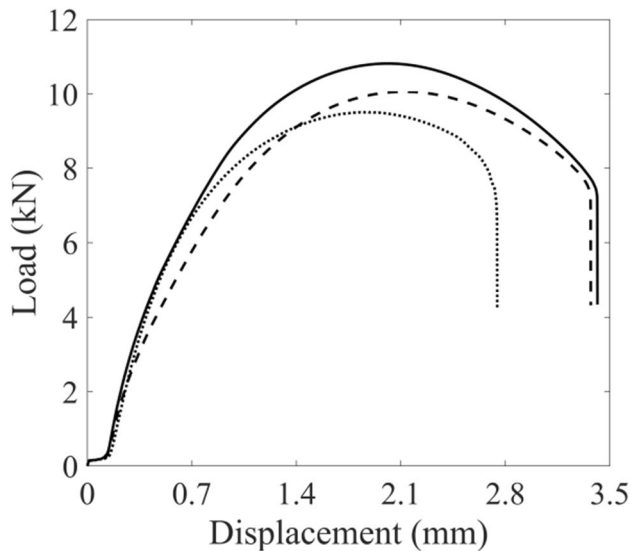


Fig. 20 Mechanical properties of the optimal welded samples

displacement (L), and failure energy (E) are 10.13 kN, 1.99 mm, and 13.85 J, respectively (Table 9). The corresponding standard deviations of them (σ_P , σ_L , and σ_E) are 0.66 kN, 0.12 mm, and 1.31 J. In conclusion, the shear tensile properties appear to faintly decrease even after optimization, which is beyond our expectations. However, the average decreased magnitude is 8.81%, which is within 10%. Besides, the improvement of the standard deviations is impressive, and the mean enhancement is 56.37%. The consuming welding heat input (Q) also decreases a lot, and its magnitude is 41.56%. Thus, the decrease in the standard deviations and welding heat input is sacrificed by the slight decrease in the mechanical attributes of the welded joints. However, it is worth sacrificing, because savings in welding heat input and significantly improved welded joints with more uniform mechanical properties are obtained.

Table 10 lists the welding quality indexes after optimization. The results were averaged from 3 samples. Table 10 shows the differences in failure energy, the depth of penetration and bottom reinforcement, and the standard deviation of absorbed energy of welded joints obtained through actual testing and regression models. The maximum relative error is within 10%, indicating the robustness and reliability of the established models in predicting and optimizing welding quality.

Table 9 The comparison of the mechanical performance of the welded samples before optimization and after optimization

Items	L	P	E	σ_L	σ_P	σ_E	Q
Unit	mm	kN	J	mm	kN	J	kJ/cm
Welded sample No. 10	2.18	10.07	16.71	0.46	0.63	5.12	7.70
Welded sample after optimization	1.99	10.13	13.85	0.12	0.66	1.31	4.50
Improvement	-8.72%	0.60%	-17.12%	99.25%	-4.55%	74.41%	41.56%

Table 10 The comparison of the welding quality based on tests and regression models

Items	E	H	σ
Unit	J	mm	J
The results achieved by the tests	13.85	3.61	1.31
The results predicted by models	13.42	3.88	1.18
Relative errors	3.10%	7.48%	9.92%

4 Conclusions

1. The welded joints produced by the various welding parameters present no major welding defects except for linear misalignment that is caused by the inaccurate assembly of the metal sheets during the GMAW process.
2. The penetration depth increases with the welding heat input until it equals the thickness of the steel sheet. Further reducing the welding speed will cause a decrease in the penetration depth but increase the bottom reinforcement geometry.
3. All the welded specimens without notches failed in the BM in the tensile tests. Their mechanical performance showed similar tendencies to that of the BM. The possession of such a high tensile strength is owing to its microstructure of AF and GBF in FZ.
4. The FZ is filled with AF, polygonal GBF, Widmanstätten ferrite, and BF, while LB, LM, GB, blocky M-A constituent (island of the second phase, composed of martensite and residual austenite), prior austenite grain boundaries, and Widmanstätten ferrite are the leading structures of CGHAZ. Due to the higher cooling rate, the amount of AF increases with the welding speed.
5. The hardness of FZ is better than that of BM. The average hardness of FZ was 240 Hv at 40.11 kJ/mm and 234 Hv at 60.84 kJ/mm. The rise in hardness is attributable to the transformation of ferrite morphology, particularly AF. The hardness steadily decreases from the HAZ to BM, while the WI and CGHAZ have the highest hardness.
6. The welded joint produced by the welding speed of 40 cm/min, the voltage of 17 V, and wire feed speed of 4.3 m/min displays excellent tensile properties (maximum displacement of 1.99 mm, peak load of 10.13 kN, and failure energy of 13.85 J) and is therefore proved to be the most suitable welding parameters for welding 3-mm-thick ASTM A606 type IV weathering steel plates.

Funding The authors express thanks to the Russian Science Foundation (22–29-20095) for the financial support.

Data availability Not applicable.

Code availability Not applicable.

Declarations

Ethics approval Since the tests and experiments in this study are not performed on humans or animals, ethical approval is unnecessary.

Consent to participate All the authors agree to participate.

Consent for publication All the authors agree to publish this article.

Conflict of interest The authors declare no conflict of interest.

References

1. Terner M, Bayarsaikhan TA, Hong HU, Lee JH (2017) Influence of gas metal arc welding parameters on the bead properties in automatic cladding. *J Weld Join* 35(1):16–25
2. Ibrahim IA, Mohamat SA, Amir A, Ghalib A (2012) The effect of gas metal arc welding (GMAW) processes on different welding parameters. *Procedia Eng* 41:1502–1506
3. Rizvi SA, Tewari SP (2017) Effect of different welding parameters on the mechanical and microstructural properties of stainless steel 304h welded joints. *Int J Eng* 30(10):1592–1598
4. Moslemi N, Redzuan N, Ahmad N, Hor TN (2015) Effect of current on characteristic for 316 stainless steel welded joint including microstructure and mechanical properties. *Procedia CIRP* 26:560–564
5. Bodude MA, Momohjimoh I (2015) Studies on effects of welding parameters on the mechanical properties of welded low-carbon steel. *J Miner Mater Charact Eng* 3(03):142
6. Wang LL, Lu FG, Wang HP, Murphy AB, Tang XH (2014) Effects of shielding gas composition on arc profile and molten pool dynamics in gas metal arc welding of steels. *J Phys D Appl Phys* 47(46):465202
7. Widyianto A, Baskoro AS, Kiswanto G, Ganeswara MF (2021) Effect of welding sequence and welding current on distortion, mechanical properties and metallurgical observations of orbital pipe welding on SS 316L. *East Eur J Enterp Technol* 2(12):110
8. Chaudhary CS, Khanna P (2021) Effect of welding parameters on the weld bead profile of submerged arc welded low carbon steel plates. *IOP Conf Ser Mater Sci Eng* 1126:012022
9. Varbai B, Kormos R, Májlinger K (2017) Effects of active fluxes in gas metal arc welding. *Period Polytech Mech Eng* 61(1):68–73
10. Ley FH, Campbell SW, Galloway AM, McPherson NA (2015) Effect of shielding gas parameters on weld metal thermal properties in gas metal arc welding. *Int J Adv Manuf Technol* 80(5):1213–1221
11. Wang L, Jin L, Huang W, Xu M, Xue J (2016) Effect of thermal frequency on AA6061 aluminum alloy double pulsed gas metal arc welding. *Mater Manuf Processes* 31(16):2152–2157
12. Hariprasath P, Sivaraj P, Balasubramanian V, Pilli S, Sridhar K (2022) Effect of the welding technique on mechanical properties and metallurgical characteristics of the naval grade high strength low alloy steel joints produced by SMAW and GMAW. *CIRP J Manuf Sci Technol* 37:584–595
13. Ribeiro HV, Baptista CA, Lima MS, Torres MA, Marcomini JB (2021) Effect of laser welding heat input on fatigue crack growth and CTOD fracture toughness of HSLA steel joints. *J Market Res* 11:801–810
14. Vaikar SJ, Narayanan V, George JC, Kanish TC, Ramkumar KD (2022) Effect of weld microstructure on the tensile properties and impact toughness of the naval, marine-grade steel weld joints. *J Market Res* 19:3724–3737
15. Kornokar K, Nematzadeh F, Mostaan H, Sadeghian A, Moradi M, Waugh DG, Bodaghi M (2022) Influence of heat input on microstructure and mechanical properties of gas tungsten arc welded HSLA S500MC steel joints. *Metals* 12(4):565
16. Noureddine M, Allaoui O (2020) Effect of tempering on mechanical properties and corrosion behavior of X70 HSLA steel weldments. *Int J Adv Manuf Technol* 106(7):2689–2701
17. Zhao D, Bezgans Y, Vdonin N, Radionova L, Bykov V (2021) Modeling and optimization of weld bead profile with varied welding stages for weathering steel A606. *Int J Adv Manuf Technol* 116(9):3179–3192
18. Chandrasekaran RR, Benoit MJ, Barrett JM, Gerlich AP (2019) Multi-variable statistical models for predicting bead geometry in gas metal arc welding. *Int J Adv Manuf Technol* 105:1573–1584
19. Jiménez-Jiménez A, Paniagua-Mercado AM, López-Hirata VM, García-Bórquez A, De Ita-De la Torre AS, Mejía-García C, Saucedo-Muñoz ML, Miguel-Díaz E (2019) Improvement of the toughness and ductility of the weld beads by inducing growth of acicular ferrite with TiO₂-nanoparticles during submerged arc welding. *Mater Res Express* 6(10):106534
20. Saha MK, Hazra R, Mondal A, Das S (2019) Effect of heat input on geometry of austenitic stainless steel weld bead on low carbon steel. *J Inst Eng India Ser C* 100(4):607–615
21. Ag K, Rv R (2021) Investigation on effects of parameters of GMAW process on bead geometry, hardness and microstructure of AISI 410 steel weldments. *Adv Mater Process Technol* 11:1–5
22. Zhao D, Bezgans Y, Vdonin N, Kvashnin V (2022) Mechanical performance and microstructural characteristic of gas metal arc welded A606 weathering steel joints. *Int J Adv Manuf Technol* 119(3):1921–1932
23. Wang XN, Zhang SH, Zhou J, Zhang M, Chen CJ, Misra RD (2017) Effect of heat input on microstructure and properties of hybrid fiber laser-arc weld joints of the 800 MPa hot-rolled Nb-Ti-Mo microalloyed steels. *Opt Lasers Eng* 91:86–96
24. Tian J, Xu G, Zhou M, Hu H (2018) Refined bainite microstructure and mechanical properties of a high-strength low-carbon bainitic steel treated by austempering below and above MS. *Steel Res Int* 89(4):1700469
25. Zhang Y, Xiao J, Liu W, Zhao A (2021) Effect of welding peak temperature on microstructure and impact toughness of heat-affected zone of Q690 high strength bridge steel. *Materials* 14(11):2981
26. Chamanfar A, Chentouf SM, Jahazi M, Lapierre-Boire LP (2020) Austenite grain growth and hot deformation behavior in a medium carbon low alloy steel. *J Market Res* 9(6):12102–12114
27. Costin WL, Lavigne O, Kotousov A (2016) A study on the relationship between microstructure and mechanical properties of acicular ferrite and upper bainite. *Mater Sci Eng A* 663:193–203
28. Zhao D, Ivanov M, Wang Y (2020) An investigation of the laser welding process for dual-phase steel via regression analysis. *IOP Conf Ser Mater Sci Eng* 969:012094
29. Ag K, Rv R (2022) Investigation on effects of parameters of GMAW process on bead geometry, hardness and microstructure of AISI 410 steel weldments. *Adv Mater Process Technol* 8:2450–2464

Publisher's note Springer Nature remains neutral with regard to jurisdictional claims in published maps and institutional affiliations.

Springer Nature or its licensor (e.g. a society or other partner) holds exclusive rights to this article under a publishing agreement with the author(s) or other rightsholder(s); author self-archiving of the accepted manuscript version of this article is solely governed by the terms of such publishing agreement and applicable law.